

A Cloud-Ozone Data Product from Aura

OMI and MLS Satellite Measurements

Jerald R. Ziemke^{1,2}, Sarah A. Strode^{2,3}, Anne R. Douglass², Joanna Joiner², Alexander Vasilkov^{2,4}, Luke D. Oman², Junhua Liu^{2,3}, Susan E. Strahan^{2,3}, Pawan K. Bhartia², David P. Haffner^{2,4}

¹Morgan State University, Baltimore, Maryland, USA

²NASA Goddard Space Flight Center, Greenbelt, Maryland, USA

³Universities Space Research Association, Columbia, MD, USA

⁴SSAI, Lanham, Maryland, USA

Abstract. Ozone within deep convective clouds is controlled by several factors involving photochemical reactions and transport. Gas-phase photochemical reactions and heterogeneous surface chemical reactions involving ice, water particles, and aerosols inside the clouds all contribute to the distribution and net production and loss of ozone. Ozone in clouds is also dependent on convective transport that carries low troposphere/boundary layer ozone and ozone precursors upward into the clouds. Characterizing ozone in thick clouds is an important step for quantifying relationships of ozone with tropospheric H_2O , OH production, and cloud microphysics/transport properties. Although measuring ozone in deep convective clouds from either aircraft or balloon ozonesondes is largely impossible due to extreme meteorological conditions associated with these clouds, it is possible to estimate ozone in thick clouds using backscattered solar UV radiation measured by satellite instruments. Our study combines Aura Ozone Monitoring Instrument (OMI) and Microwave Limb Sounder (MLS) satellite measurements to generate a new research product of monthly-mean ozone concentrations in deep convective clouds between 30°S to 30°N for October 2004 – April 2016. These measurements represent mean ozone concentration primarily in the upper levels of thick clouds and reveal key

30 features of cloud ozone including: persistent low ozone concentrations in the tropical Pacific of
31 ~10 ppbv or less; concentrations of up to 60 pphv or greater over landmass regions of South
32 America, southern Africa, Australia, and India/east Asia; connections with tropical ENSO
33 events; and intra-seasonal/Madden-Julian Oscillation variability. Analysis of OMI aerosol
34 measurements suggests a cause and effect relation between boundary layer pollution and
35 elevated ozone inside thick clouds over land-mass regions including southern Africa and
36 India/east Asia.

37

38 **1. Introduction.**

39

40 Measuring tropospheric ozone in deep convective clouds including convective outflow regions in
41 the mid-upper troposphere is important for several reasons. Ozone in the upper troposphere is a
42 major greenhouse gas that contributes to climate forcing. The IPCC 2013 Report (e.g., in
43 Hartmann et al., 2014; <http://www.ipcc.ch/report/ar5/wg1/>) includes an evaluation of
44 tropospheric versus stratospheric ozone using a collage of radiative transfer model calculations.
45 The report shows that the radiative forcing of tropospheric ozone is 10 times greater than that of
46 stratospheric ozone, even though only 10% of the atmospheric ozone resides in the troposphere.
47 The IPCC 2013 report (and references therein) also notes that ozone is a major surface pollutant,
48 and is important as the main source of OH, the primary cleanser of pollutants in the troposphere.
49 Measurements of ozone associated with deep convection are needed to characterize the extent of
50 ozone inter-relationships with tropospheric H₂O and OH production, and in understanding cloud
51 microphysics/transport properties and resulting influence on global and regional tropospheric
52 ozone distributions.

53

54 Microphysics and photochemistry can be very complex for deep convective clouds. Huntrieser
55 et al. (2016, and references therein) combined aircraft and cloud measurements with a model to
56 study ozone distributions and sources associated with deep convective clouds over the central
57 U.S. Huntrieser et al. (2016) identified upward transport of lower tropospheric ozone and ozone
58 precursors into the upper troposphere within thick clouds. They also showed that cloud tops
59 over-shoot the tropopause and inject high amounts of biomass burning pollutants (largely CO
60 and NO_x) and lightning-produced NO_x into the low stratosphere, while at the same time ozone-

61 rich air from the low stratosphere is transported downward into the cloud anvil and surrounding
62 outflow regions as a dynamical response to overshooting. Some of the Geostationary
63 Operational Environmental Satellite (GOES) cloud tops were found to reach up to 17-18 km
64 altitude for these deep convective systems. Pronounced ozone-rich stratospheric air was
65 observed within cloud outflow regions.

66

67 The ozonesonde measurement record includes occurrences of very low to even “near-zero”
68 ozone concentrations in the tropical upper troposphere associated with the passing of deep
69 convective cloud systems (e.g., Kley et al., 1996; Folkins et al., 2002; Solomon et al., 2005).
70 The very low ozone values are largely attributed to convective lifting of low concentrations of
71 ozone from the marine boundary layer into the upper troposphere. In pollution-free oceanic
72 regions it is not uncommon for ozone in the marine boundary layer to be only a few ppbv due to
73 ozone net loss reactions involving hydrogen radicals OH and HO₂ (e.g., Solomon et al., 2005,
74 and references therein). Some studies suggest the possibility of in-cloud photochemical ozone
75 destruction mechanisms (e.g., Zhu et al., 2001; Barth et al., 2002; Liu et al., 2006). Vömel and
76 Diaz (2010) showed that improperly calibrated Electrochemical Concentration Cell (ECC)
77 ozonesondes led to a small measurement error (under-determination) and the near-zero upper
78 troposphere ozone concentrations reported in these studies. Vömel and Diaz (2010) found that
79 the near-zero ozone concentrations in the upper troposphere were instead about 10 ppbv and
80 attributed the calibration error to unaccounted variations associated with background cell
81 currents at launch. Vömel and Diaz (2010) indicate that the studies measuring “near-zero” ozone
82 were not wrong, but instead slightly underdetermined the low ozone concentrations.

83

84 The very low ozone measurements in the tropical upper troposphere in past studies were
85 obtained from a limited number of aircraft flights and ozonesondes at a few isolated sites in the
86 vicinity of, but not inside, deep convective cloud systems. Measuring ozone directly inside deep
87 convective clouds from ozonesondes and aircraft instruments remains an elusive task due to
88 extreme meteorological conditions associated with the clouds. Ziemke et al. (2009) developed a
89 residual “cloud slicing” method for measuring ozone volume mixing ratios within thick clouds
90 by combining Aura Ozone Monitoring Instrument (OMI) and Microwave Limb Sounder (MLS)
91 satellite measurements. For deep convective clouds, OMI provided the tropospheric cloud ozone

92 measurements after subtracting co-located MLS stratospheric column ozone. Their study found
93 large variability in the ozone concentrations in thick clouds. While very low ozone
94 concentrations (< 10 ppbv) in the clouds were identified in the remote Indian and Pacific Ocean
95 regions, concentrations greater than 60 ppbv were obtained over continental landmasses
96 including Africa. Ziemke et al. (2009) hypothesized that the ozone measured in thick clouds is
97 largely a manifestation of ozone concentrations (from low to high amounts) present in the low
98 troposphere/boundary layer that become transported upward by convection.

99

100 We build upon the cloud slicing work of Ziemke et al. (2009) to produce a long data record of
101 OMI/MLS cloud ozone measurements as that former study was limited to only a few months
102 during 2005 and 2006. As with Ziemke et al. (2009), we derive ozone mixing ratios inside
103 tropical deep convective clouds by combining Aura OMI measurements of total column ozone
104 and cloud pressure with Aura MLS stratospheric column ozone. The ozone measurements
105 represent mean ozone concentrations in the upper levels of the clouds above 550 hPa. This paper
106 is organized as follows: Section 2 details the satellite measurements while Section 3 is an
107 overview of cloud slicing. Section 4 discusses validation and Sections 5-6 discuss basic
108 characteristics and scientific interpretations of the data. Finally, Section 7 provides a summary.

109

110 **2. Satellite Measurements.**

111

112 Our study combines Aura OMI and MLS ozone measurements with OMI aerosols and cloud
113 parameters (i.e., cloud pressures, radiative cloud fractions). OMI is a UV/VIS solar backscatter
114 spectrometer that makes daily measurements of Earth radiances and solar irradiances from 270 to
115 500 nm with spectral resolution of about 0.5 nm (Levelt et al., 2006). OMI scans perpendicular
116 to the orbit path with 60 side-scan positions and provides near-global coverage of the sunlit Earth
117 with a pixel size of 13 km × 24 km at nadir. The current OMI total ozone that we use is derived
118 using a v8.5 algorithm. Description and access to the OMI v8.5 data can be obtained from the
119 website <http://disc.sci.gsfc.nasa.gov/Aura/data-holdings/OMI>. In January 2009 a physical
120 external optical blockage known as the “row anomaly” reduced the number of the 60 good side-
121 scanning row measurements to about 30-40. Scan positions 21-55 are the most affected, with

122 dependence on latitude and specific day. All of the OMI measurements that we use were
123 properly screened to exclude all data affected by the row anomaly artifact.

124

125 OMI cloud pressures and radiative cloud fractions are derived using UV-2 radiances (Vasilkov et
126 al., 2008). The cloud pressure from OMI is named optical centroid pressure (OCP). As shown
127 by Vasilkov et al. (2008), the OCP at UV wavelengths lies deep inside the clouds, often by
128 several hundred hPa and therefore is not a measure of true cloud top; they showed this by
129 comparing the OMI OCP measurements with both Cloudsat radar reflectivity profiles and
130 MODIS IR cloud pressures. The OCP effectively represents the bottom reflecting surface for the
131 OMI retrievals in the presence of clouds. The true ozone measurement from OMI is the column
132 amount from the top of the atmosphere down to the reflecting surface. In the presence of a
133 cloud, the OMI algorithm places an ozone “ghost column” climatology estimate below the OCP
134 reflecting surface to obtain total column ozone.

135

136 There are two OMI algorithms that determine the OCP. The first algorithm is based on O₂-O₂
137 dimer absorption (Sneep et al., 2008) and the second is based on rotational-Raman scattering
138 (RRS) that uses spectral structures in the ratio of backscattered radiance to solar irradiance,
139 known as the Ring effect (Joiner and Bhartia, 1995; Joiner et al., 2004; Joiner and Vasilkov,
140 2006, Joiner et al., 2012). The two OMI cloud algorithms provide similar estimates of OCP for
141 bright clouds although there are small differences due to algorithmic and physical effects (Sneep
142 et al., 2008). We use the RRS cloud pressure for our study although our results would be nearly
143 identical using the O₂-O₂ cloud measurements. We refer to “cloud ozone” as the ozone column
144 or ozone mean volume mixing ratio lying between the tropopause and retrieved OCP from OMI
145 under conditions of deep convection. We also refer to “above-cloud ozone” as the ozone column
146 measured from OMI lying from the top of the atmosphere down to the OMI OCP. Deep
147 convective clouds often have cloud tops at or near the tropopause. Therefore much if not most of
148 the tropospheric ozone measured between the tropopause and OMI cloud pressure lie within the
149 cloud itself rather than above the cloud top.

150

151 Aura MLS v4.2 profile ozone is included to measure fields of stratospheric column ozone (SCO).
152 MLS SCO is used in conjunction with OMI above-cloud column ozone each day to derive mean

153 column amounts and mean concentrations of ozone measured over deep convective clouds. The
154 MLS ozone profiles are vertically integrated in log-pressure from 0.0215 hPa down to the
155 tropopause to derive measurements of SCO as described by Ziemke et al. (2006, 2009). To
156 separate stratospheric from tropospheric ozone we similarly use the WMO $2\text{K}\cdot\text{km}^{-1}$ lapse-rate
157 tropopause pressure definition with NCEP re-analysis temperatures. Other tropopause pressure
158 definitions and other meteorological analyses besides NCEP could have also been used. We
159 included the WMO definition with NCEP for both historical reasons and consistency checking
160 relative to previous versions of our OMI/MLS tropospheric ozone products that used the same
161 NCEP tropopause. For the low latitudes in our study we expect that there would be only minor
162 differences in our results if we used instead a different tropopause. All MLS v4.2 retrieval
163 quality flags (quality, status, convergence, and precision) are properly adhered to for all of our
164 analyses. The MLS v4.2 measurements including data quality and quality flags are described in
165 the MLS data quality document http://mls.jpl.nasa.gov/data/v4-2_data_quality_document.pdf.
166 Recommended pressure levels for science applications with MLS v4.2 ozone are 0.0215 hPa to
167 261 hPa. There are errors in derived SCO from MLS caused by both errors in NCEP tropopause
168 pressure and MLS data themselves. The MLS v4.2 data quality document indicates that the
169 vertical resolution for MLS about the tropopause is about 3 km. This resolution is very good
170 when compared to other current instruments for isolating stratospheric columns, particularly
171 nadir profilers such as the NOAA Solar Backscatter Ultraviolet Spectrometer (SBUV)
172 instrument that has vertical resolution about the tropopause \sim 10-12 km. Although the resolution
173 is much better for MLS it will still affect daily SCO measurements by possibly adding errors of
174 several DU. We average all daily measurements over a month which will reduce these errors if
175 random; however, it is likely that there is a component of unresolved systematic error which will
176 not be reduced by this averaging.

177

178 **3. Overview of Cloud Slicing.**

179

180 We use two cloud slicing methods to measure cloud ozone from Aura OMI and MLS
181 instruments. The first method is called “ensemble” cloud slicing that uses daily co-located
182 measurements of cloud pressure and column ozone. This algorithm was first proposed by
183 Ziemke et al. (2001) and combined co-located Nimbus-7 TOMS column ozone and THIR IR

184 cloud-top pressure. Here we combine OMI column ozone with OMI cloud pressure (i.e., OCP).
185 An advantage of ensemble cloud ozone is that it requires only a single instrument, but
186 weaknesses are noisiness and poor spatial resolution in the measurements. The second method is
187 a residual cloud slicing approach (Ziemke et al., 2009) that combines OCPs from OMI with
188 residual column ozone differences between OMI and MLS. An advantage of the residual
189 method is that it can yield measurements with high horizontal resolution. The cloud ozone
190 product that we generate comes from the OMI/MLS residual method. We use OMI ensemble
191 measurements only as a consistency check for the OMI/MLS residual ozone.

192

193 A schematic diagram for the ensemble cloud slicing method is shown in Figure 1. A region is
194 first chosen (top of figure, $5^\circ \times 5^\circ$ region shown) with all coincident measurements (either daily
195 or daily measurements accumulated over a month) of OMI above-cloud column ozone plotted
196 versus OCP effective cloud pressure (bottom of figure). The OCP as noted in Section 2 may lie
197 several hundred hPa below the cloud top, and the OMI algorithm places a climatological ozone
198 ghost column below the OCP to determine total column ozone. For cloud slicing we use only the
199 above-cloud ozone from OMI which is the true measurement. In practice, we determine the
200 above-cloud column ozone by subtracting the ghost column ozone from total column ozone
201 reported in the OMI level-2 orbital datasets.

202

203 In Figure 1 the OMI footprint scene depicted is 100% cloud filled so that the OCP deep inside
204 the cloud represents the bottom reflecting surface for the OMI retrieval. In the more common
205 case involving clouds, footprint scenes from OMI will not be 100% cloud filled and we account
206 for this. What we generally use for cloud slicing in the Figure 1 schematic is an effective scene
207 pressure (P_{EFF}) in place of the OCP. P_{EFF} is derived from $P_{EFF} = P_{CLOUD} \cdot f + P_{SURFACE} \cdot (1-f)$,
208 where P_{CLOUD} is the cloud OCP, $P_{SURFACE}$ is the Earth surface scene pressure, and f is the OMI
209 scene radiative cloud fraction (Joiner et al., 2009). We simplify our cloud slicing method (as
210 was done by Ziemke et al. 2009) by using OMI measurements only when OMI reflectivity is
211 greater than 0.80. Choosing only OMI reflectivity scenes greater than 0.8 ensures that f is equal
212 to 1.0, and thus P_{EFF} is equivalent to OCP for all of our cloud slicing measurements. We note
213 that the deep convective clouds we incorporate generally have physical cloud tops at or near

214 tropopause level with OCPs in the mid-upper troposphere; in such case the derived mixing ratio
215 from cloud slicing is primarily an average measurement of ozone inside the upper levels of
216 clouds.

217

218 Tropospheric ozone mean volume mixing ratio (VMR) is estimated by fitting a straight line to
219 the data pairs of above-cloud column ozone versus OCP over the selected geographical region.
220 This method was first described by Ziemke et al. (2001) and is summarized here. Column ozone
221 ($\Delta\Omega$) between two altitudes z_1 and z_2 is by definition the number of molecules per unit
222 horizontal area and is calculated by integrating ozone number density n as $\Delta\Omega = \int_{z_1}^{z_2} n \cdot dz$. Using
223 hydrostatic balance $\partial P / \partial z = -\rho g$ (ρ is mass density, g is acceleration of gravity) and assuming
224 an invariant acceleration of gravity for the troposphere this expression can be converted to: $\Delta\Omega$
225 (in Dobson Units, DU; 1 DU = 2.69×10^{20} molecules-m⁻²) = $C \cdot \int_{P_1}^{P_2} X \cdot dP = C \cdot \bar{X} \cdot (P_2 - P_1)$,
226 where $C = 0.00079$ DU-hPa⁻¹-ppbv⁻¹ and \bar{X} is ozone mean VMR in units ppbv. It follows that
227 ozone mean VMR in the troposphere is \bar{X} (ppbv) = $1270 \cdot \Delta\Omega / \Delta P$, or in other words 1270
228 multiplied by the slope of the ensemble line fit. The 2σ uncertainty for VMR in ppbv is
229 determined by multiplying the calculated 2σ uncertainty of the slope by 1270. An estimate for
230 SCO can also be obtained by extrapolating the line fit to the mean tropopause pressure over the
231 region. The above-cloud ozone at the extrapolated tropopause pressure, a direct estimate of
232 SCO, can be compared with MLS SCO to assess how well the ensemble method separates
233 stratospheric from tropospheric column ozone.

234

235 An example of ensemble scatter plots is shown in Figure 2 for October 5, 2008. The left scatter
236 plot coincides with the region of southern Africa while the right scatter plot coincides with the
237 western Pacific. Measured ozone mixing ratio is 72 ppbv over southern Africa and 10 ppbv over
238 the western Pacific. The enhanced ozone over southern Africa suggests that ozone produced
239 from regional pollution including biomass burning, which is largest around September-October
240 each year in the SH, reaches the upper regions of the clouds. However, the regional elevated
241 ozone over southern Africa may be caused by other sources including lightning NO_x, and
242 transport by the Walker circulation, and mixing of stratospheric air that is transported into the

243 troposphere in response to cloud tops overshooting the tropopause (e.g., Huntrieser et al., 2016,
244 and references therein). The low ozone VMR in the western Pacific in Figure 2 is consistent
245 with low values measured in the vicinity of tropical deep convection by ozonesondes (e.g., Kley
246 et al., 1996; Folkins et al., 2002; Solomon et al., 2005; Vömel and Diaz, 2010). In principle we
247 derive monthly cloud ozone measurements instead of daily from the ensemble method by
248 accumulating all co-located daily data pairs over a month.

249

250 Figure 3 illustrates the residual technique for measuring cloud ozone. This method combines
251 OMI above-cloud column ozone and OMI OCP with MLS SCO. All of these combined
252 measurements are daily and are co-located. For a deep convective cloud the OCP lies well inside
253 the cloud with a cloud top often at or near the tropopause, so that much or most of measured
254 tropospheric ozone lies inside the cloud rather than above the cloud top. The relationship (Joiner
255 et al., 2009) to derive residual cloud ozone VMR (units ppbv) is
256 $VMR = 1270 \cdot [\Delta\Omega / (P_{EFF} - P_{TROPOPAUSE})]$, where $\Delta\Omega$ is the difference (in DU) of OMI above-
257 cloud column ozone minus MLS SCO, $P_{TROPOPAUSE}$ is tropopause pressure (in hPa), and P_{EFF} is
258 the effective scene pressure (also in hPa) as discussed above. The number 1270 is the same as
259 for the ensemble method to ensure units ppbv for VMR. As a final step, monthly-mean residual
260 values are derived from the daily residual measurements.

261

262 We limit the latitude range for both the ensemble and residual methods to 30° S - 30° N. This
263 was done for both approaches to reduce inherent noise due in part to strong dynamical variability
264 of the tropopause from the tropospheric wind jets.

265

266 **4. OMI/MLS Residual Cloud Ozone Product: Validation and Consistency Checks.**

267

268 The validation of OMI/MLS residual cloud ozone measurements is not straightforward given the
269 paucity of in-cloud measurements from independent sources such as ozonesondes and aircraft.
270 However, as one approach similar to Ziemke et al. (2009), we can still obtain at least a
271 consistency check between the OMI/MLS residual cloud ozone and cloud ozone obtained from
272 the OMI-only ensemble method.

273

274 Figure 4 compares cloud ozone from the ensemble and residual techniques for July 2015 (left
275 panel) and October 2015 (right panel). Both of these months coincide with the intense 2014-
276 2016 El Nino. The two panels in Figure 4 each compare OMI/MLS residual cloud ozone (thick
277 curves) and OMI ensemble cloud ozone (asterisks). The 5°S-10°N latitude band was chosen
278 because it includes much of the ITCZ with thick clouds for these months. Both the ensemble and
279 residual cloud ozone in Figure 4 are low to near zero in the eastern and western Pacific close to
280 the dateline; it is conceivable that these oceanic regions coincide generally with pristine air and
281 low concentrations of both ozone and ozone precursors in the boundary layer. In contrast, over a
282 broad region extending from the western Pacific to Indonesia the cloud ozone from both
283 measurements is enhanced. The increased tropospheric ozone is due to a combination of
284 suppressed convection during El Nino and increases in biomass burning over Sumatra and
285 Borneo due to the induced dry conditions and wildfires (e.g., Chandra et al., 1998; Logan et al.,
286 2008). The suppressed convection during El Nino coincides with reduced upward injection of
287 low ozone concentrations in the oceanic boundary layer compared to non-El Nino years, thus
288 contributing to anomalous increase in cloud ozone relative to non-ENSO years. In the central
289 Atlantic the cloud ozone measurements are ~50 ppbv for both methods indicating higher ozone
290 concentrations injected into the clouds from below and in general a more polluted region
291 compared to the Pacific. In the eastern Atlantic extending to the Indian Ocean / western Pacific
292 (i.e., ~60°–120 °) the ensemble measurements are larger than for OMI/MLS. The calculated $\pm 2\sigma$
293 uncertainties for the ensemble measurements are large everywhere including this broad region
294 and illustrate the noisy nature of the ensemble method due largely to sparseness of thick clouds.
295 Unlike measurements for the OMI/MLS residual method, large errors in ozone for the ensemble
296 method may originate largely from the basic assumptions of the methodology such as uniformity
297 of both SCO and tropospheric mixing ratio throughout the chosen region. In the next two
298 sections we discuss the OMI/MLS cloud ozone product for basic geophysical characteristics
299 including some science results.

300

301 **5. Monthly Distributions.**

302

303 Figure 5 shows monthly-mean climatology maps of OMI/MLS residual cloud ozone derived
304 from averaging similar months over the long record. Plotted in Figure 5 is mean VMR (units
305 ppbv) representing average ozone concentration lying between the tropopause and OMI OCP as
306 described in Section 3. In Figure 5 the mean mixing ratio is calculated for OCPs varying
307 between 250 hPa and 550 hPa. We have chosen this OCP pressure band to help isolate optically
308 thick clouds with cloud tops generally at or near tropopause level (e.g., see Figure 12 of Vasilkov
309 et al., 2008). The black regions in Figure 5 indicate not enough deep convective clouds present
310 and/or mostly clouds such as low-marine stratus clouds with OCP lying below the 550 hPa
311 threshold.

312

313 The distributions in Figure 5 illustrate the large regional and temporal variability present in
314 cloud-ozone. In the remote Pacific and Indian Ocean regions the values of cloud ozone are small
315 at ~10 ppbv or less. High values reaching 70-80 ppbv are measured for landmass regions of
316 India/east Asia, southern Africa and South America, and Australia. The high ozone is indicative
317 of a more polluted lower troposphere/boundary layer. There are also some ozone values ~40-50
318 ppbv over both the Atlantic and Pacific Ocean regions in higher latitudes which are large yet still
319 small compared to the noted high values over landmasses. Understanding variations in the ozone
320 concentrations over oceanic thick clouds is work in progress that combines these OMI/MLS
321 measurements with a free-running chemistry-climate model (Strode et al., 2017).

322

323 Figure 6 shows climatology maps similar to Figure 5 but instead for “background” ozone mean
324 VMR. The background ozone is derived using only OMI near clear-sky scenes for column
325 ozone where radiative cloud fractions are less than 30%. In Figure 6 the east-west tropical wave-
326 1 pattern in tropospheric ozone (Fishman et al., 1990) is easily discerned year round with high
327 values ~60-80 ppbv in the Atlantic and low values ~20 ppbv in the eastern and western Pacific.
328 According to Sauvage et al. (2007) using the GEOS-Chem Chemical Transport Model (CTM)
329 the main source of tropospheric ozone in the tropical Atlantic on annual-mean basis comes from
330 lightning NO_x with smaller contributions from biomass burning, soils, and fossil fuels (by factors
331 varying ~4-6). Their CTM also indicated that stratosphere-troposphere exchange (STE) accounts
332 for less than about 5% of tropospheric ozone burden in the tropical Atlantic and that most of the
333 effects from NO_x came from Africa. In the SH subtropics in Figure 6 there is a buildup of high

334 ozone in August-November along all longitudes. Although the SH Atlantic maximum in Figure
335 6 occurs in every month year round, this feature also exhibits substantial inter-annual variability.
336 Liu et al. (2017) combined GEOS-5 assimilated OMI/MLS ozone and Goddard Modeling
337 Initiative (GMI) CTM simulations to quantify the causes of the inter-annual variability (IAV) of
338 tropospheric ozone over four sub-regions of the southern hemispheric tropospheric ozone
339 maximum. They found that the strong influence of emission on ozone IAV is largely confined to
340 the South Atlantic region in September at and below ~430 hPa. In the middle and upper
341 troposphere, the IAV of the stratospheric ozone contribution is the most important factor driving
342 the IAV of ozone over two selected tropical regions: the tropical south Atlantic and tropical S. E.
343 Pacific, especially during the austral winter season.

344

345 **6. Time Series.**

346

347 With about 12 years of measurements from OMI/MLS we can analyze variability from monthly
348 to decadal timescales of the OMI/MLS residual cloud ozone and compare these changes with
349 background ozone. In Figure 7 we show eight selected regions of interest for background ozone
350 (top) and cloud ozone (bottom) for October 2006. For these eight selected regions we have
351 averaged cloud ozone and background ozone each month to generate long-record time series
352 starting October 2004.

353

354 Time series of the monthly background ozone and cloud ozone for the eight regions are plotted
355 in Figures 8 and 9. In all of these eight panels the background ozone is plotted as the thick solid
356 curve while cloud ozone is the thin curve with asterisks. Also plotted for the six landmass
357 regions in Figures 8-9 are time series of the OMI aerosol index (dotted blue curves). In Figure 8
358 for northern Africa we include a line plot of the solar MgII UV index (blue squares) for
359 comparing decadal changes in ozone in all eight panels in Figures 8-9 with the 11-year solar
360 cycle. In the eastern Pacific region in Figure 9 the Nino 3.4 index (blue squares) is also plotted
361 to demonstrate the dependence of cloud ozone variability from ENSO in this particular region.
362 All background ozone and aerosol time series in Figures 8-9 were flagged missing wherever (at
363 $1^\circ \times 1.25^\circ$ gridding) and whenever (monthly means) corresponding measurements for cloud ozone
364 were missing.

365
366 Figure 8 compares ozone time series for the following four regions: Central America, South
367 America, northern Africa, and southern Africa. In each panel the correlation between cloud
368 ozone and background ozone is shown. In addition the correlation between cloud ozone and
369 aerosols is also included for southern Africa. With the exception of the southern Africa region,
370 the background ozone is larger than cloud ozone by ~10-20 ppbv year round. For southern
371 Africa the cloud ozone each year in summer months exceeds background ozone by ~5-10 ppbv
372 on average. The annual cycle for cloud ozone with southern Africa does not appear to be in
373 phase with background ozone, reaching its annual maximum about 1-2 months earlier. The
374 aerosol index time series in Figure 8 for southern Africa represents seasonality of biomass
375 burning in the region and it also peaks 1-2 months prior to maximum background ozone; the
376 correlation between cloud ozone and aerosols shown in this panel for southern Africa is about
377 0.63. Sporadic thick clouds in the presence of tropospheric ozone from biomass burning via
378 nearby regions may explain the higher ozone values and 1-2 month phase lead for cloud ozone
379 relative to background ozone.
380
381 With Central America in Figure 8 (upper left panel) some of the month-to-month maxima and
382 minima for cloud ozone coincide with relative maxima and minima in background ozone on
383 intra-seasonal time scale. The Central America region including the Caribbean Sea/Gulf of
384 Mexico and extending into the tropical north Atlantic is well documented for intra-seasonal
385 variability in winds and cyclonic development (e.g., Park and Schubert, 1993; Maloney and
386 Hartmann, 2000; Mo, 2000; Foltz and McPhaden, 2004, 2005). Seasonal variability in Figure 8
387 for both background ozone and cloud ozone is most pronounced for southern Africa and weakest
388 for northern Africa.
389
390 For decadal time scale, the background ozone in all four regions in Figure 8 is mostly invariant
391 while cloud ozone shows small decreases toward the middle of the record followed by small
392 increases afterward. Comparing with the MgII index in the upper right panel, this decadal
393 variability for cloud ozone does not appear to be directly related to the 11-year cycle in solar UV
394 which has minima centered around year 2009 and also at the end of the record.
395

396 Figure 9 shows time series for four additional regions: India/east Asia, Indonesia, eastern Pacific,
397 and Australia. With the exception of Australia (lower right panel), the background ozone is
398 larger than cloud ozone by ~10-20 ppbv year round. The cloud ozone and background ozone for
399 Australia are comparable during July-November months (i.e., similar to southern Africa in
400 Figure 8). For Indonesia and the eastern Pacific the cloud ozone is sometimes very low to even
401 near zero which is indicative of clean air with low concentrations of boundary-layer ozone and
402 ozone precursors. Indonesia in Figure 9 indicates intra-seasonal variability for both cloud ozone
403 and background ozone. In this western pacific region the main source of intra-seasonal
404 variability of tropospheric ozone is the 1-2 month Madden-Julian Oscillation (e.g., Ziemke et al.,
405 2015, and references therein).

406

407 Decadal changes of cloud ozone in Figure 9, with the exception of the eastern Pacific, appears
408 again to have relative minima around the middle of the long record and no clear connection with
409 the 11-year solar cycle in UV. Included in the panel for the eastern Pacific region is the Nino 3.4
410 index time series (squares along bottom) which was re-scaled for plotting with the ozone. For
411 the eastern Pacific it is clear that there is dominant inter-annual variability related to ENSO
412 events with associated changes in convection/SST (i.e., opposite correlation between them is
413 indicated). For this eastern Pacific region the cloud ozone is greatest during La Nina (suppressed
414 convection in the region) and lowest during El Nino (enhanced convection in the region).

415

416 It is difficult to discern timing of the seasonal minima and maxima of the aerosol and ozone time
417 series in Figures 8-9. For this reason we have included Figure 10 that compares 12-month
418 climatologies of background ozone, cloud ozone, and aerosol index time series for the six
419 landmass regions plotted in Figures 8-9. One main conclusion from Figure 10 is that seasonal
420 maxima of background ozone for the landmass regions of southern Africa, India/east Asia, and
421 Australia all tend to occur about one month after maxima in aerosols. For southern Africa and
422 India/east Asia the aerosol maximum occurs around the same month as the maximum in cloud
423 ozone. These phase shifts suggest that biomass burning during the mostly dry season has an
424 important impact on the seasonal cycles of tropospheric ozone including India where monsoon
425 does not generally begin until late May or early June. It is beyond the scope of our study to
426 explain the relative amplitude differences and phase shifts between background and cloud ozone

427 measurements. Explaining these characteristics will require a future investigation using either a
428 chemical transport model or a chemistry-climate model with an appropriate convection scheme.

429

430 **7. Summary.**

431

432 We applied a residual technique to derive a data record (October 2004-recent) of tropospheric
433 ozone mixing ratios inside deep convective clouds in the tropics and subtropics from OMI/MLS
434 satellite measurements. This residual technique makes use of the cloud optical centroid pressure
435 (OCP) obtained from the effects of rotational-Raman scattering in the OMI UV spectra. Solar
436 UV penetrates deep into thick clouds, often by several hundred hPa. In addition, deep
437 convective clouds have high cloud tops often near or at tropopause level. As a result the
438 OMI/MLS cloud ozone measurements are largely indicative of ozone concentrations lying inside
439 the clouds.

440

441 The OMI/MLS residual cloud ozone was compared with OMI/MLS near clear-sky ozone
442 (denoted “background” ozone) indicating substantially lower concentrations (by ~10-20 ppbv)
443 for cloud ozone year round, with the exception of southern Africa and Australia during July-
444 November months. For both southern Africa and Australia the seasonal maxima of cloud ozone
445 was found to exceed seasonal maxima of background ozone by about 5-10 ppbv. For both
446 southern Africa and India/east Asia the seasonal maxima for both OMI aerosols and cloud ozone
447 occurs about 1-2 months earlier than for background ozone. The analyses imply a cause and
448 effect relation between boundary layer pollution and elevated ozone inside thick clouds over
449 land-mass regions including southern Africa and India/east Asia.

450

451 While large cloud ozone concentrations ~60 ppbv or greater occur over landmass regions of
452 India/east Asia, South America, southern Africa, and Australia, very low cloud ozone is
453 persistent over the Indian Ocean and eastern/western Pacific Ocean with values ~10 ppbv or
454 smaller. A low concentration of cloud ozone measured in these oceanic regions is indicative of
455 generally pristine air with small amounts of ozone and ozone precursors in the marine boundary
456 layer/low troposphere.

457

458 There is indication of intra-seasonal variability in cloud ozone over the eastern and western
459 Pacific Ocean regions and also over Central America. In the western Pacific the intra-seasonal
460 variability originates largely from the 1-2 month Madden-Julian Oscillation. In the eastern
461 Pacific the largest variability is inter-annual and originates from ENSO and associated changes
462 in SST/convection. In the eastern Pacific the highest cloud ozone occurs during La Nina
463 (suppressed convection over the region) with lowest cloud ozone during El Nino (enhanced
464 convection).

465

466 Understanding changes in convection versus changes in emissions and how they relate to the
467 variabilities in measured cloud ozone is beyond the scope of our study. A photochemical model
468 involving deep convective clouds would be necessary to study the variability for cloud ozone
469 from monthly to decadal time scale. Strode et al. (2017) is current work in progress that
470 combines these OMI/MLS measurements with a chemistry-climate model to evaluate properties
471 of cloudy versus clear-sky background ozone.

472

473 The monthly gridded cloud ozone and background ozone data can be obtained via anonymous ftp
474 from the following:

475

476 > ftp jwocky.gsfc.nasa.gov
477 > Name: anonymous
478 > Password: (your email address)
479 > cd pub/ccd/data_monthly
480 > get vmr_30s_to_30n_oct04_to_apr16.sav

481

482

483

484 **Acknowledgments.** The authors thank the Aura MLS and OMI instrument and algorithm teams
485 for the extensive satellite measurements used in this study. OMI is a Dutch-Finnish contribution
486 to the Aura mission. Funding for this research was provided in part by NASA
487 NNH14ZDA001N-DSCOVR.

488

489
490
491
492
493
494
495

496 **References.**

497
498
499
500

Barth, M. C., P. G. Hess, and S. Madronich, Effect of marine boundary layer clouds on tropospheric chemistry as analyzed in a regional chemistry transport model, *J. Geophys. Res.*, 107, (D11), 4126, 2002.

501

502 Chandra, S., J. R. Ziemke, W. Min, and W. G. Read, Effects of 1997-1998 El Nino on
503 tropospheric ozone and water vapor, *Geophys. Res. Lett.*, 25, 3867-3870, 1998.

504

505 Fishman, J., C. E. Watson, J. C. Larsen, and J. A. Logan, Distribution of tropospheric ozone
506 determined from satellite data, *J. Geophys. Res.*, 95(D4), 3599-3617, 1990.

507

508 Folkins, I., C. Braun, A. M. Thompson, and J. Witte, Tropical ozone as an indicator of deep
509 convection, *J. Geophys. Res.*, 107 (D13), doi:10.1029/2001JD001178, 2002.

510

511 Foltz, G. R., and M. J. McPhaden, The 30–70 day oscillations in the tropical Atlantic, *Geophys.*
512 *Res. Lett.*, 31, L15205, doi:10.1029/2004GL020023, 2004.

513

514 Foltz, G. R., and M. J. McPhaden, Mixed layer heat balance on intra-seasonal time scales in the
515 northwestern tropical Atlantic Ocean, *J. Clim.*, 18(20), 4168 – 4187, 2005.

516

517 Hartmann, D. L., A. M. G. Klein Tank, M. Rusticucci, L. V. Alexander, S. Brönnimann, Y. Charabi,
518 F. J. Dentener, E. J. Dlugokencky, D. R. Easterling, A. Kaplan, B. J. Soden, P. W. Thorne, M. Wild
519 and P. M. Zhai,, Observations: Atmosphere and Surface. In: *Climate Change 2013: The Physical*

520 Science Basis. Contribution of Working Group I to the Fifth Assessment Report of the
521 Intergovernmental Panel on Climate Change [Stocker, T. F., D. Qin, G.-K. Plattner, M. Tignor, S. K.
522 Allen, J. Boschung, A. Nauels, Y. Xia, V. Bex, and P.M. Midgley (eds.)], Cambridge University
523 Press, Cambridge, United Kingdom and New York, NY, USA, 2014.

524

525 Huntrieser, H., et al., On the origin of pronounced O₃ gradients in the thunderstorm outflow
526 region during DC3, *J. Geophys. Res. Atmos.*, 121, 6600–6637, doi:10.1002/2015JD024279,
527 2016.

528

529 Joiner J., and P. K. Bhartia, The determination of cloud pressures from rotational-Raman
530 scattering in satellite backscatter ultraviolet measurements. *J. Geophys. Res.*, 100, 23,019-
531 23,026, 1995.

532

533 Joiner, J., A. P. Vasilkov, D. E. Flittner, J. F. Gleason, and P. K. Bhartia, Retrieval of cloud
534 pressure and oceanic chlorophyll content using Raman scattering in GOME ultraviolet spectra, *J.*
535 *Geophys. Res.*, 109, D01109, doi:10.1029/2003JD003698, 2004.

536

537 Joiner, J., and A. P. Vasilkov, First results from the OMI rotational Raman scattering cloud
538 pressure algorithm, *IEEE Trans. Geosci. Rem. Sens.*, 44, 1272-1282, 2006.

539

540 Joiner, J., M. R. Schoeberl, A. P. Vasilkov, L. Oreopoulos, S. Platnick, N. J. Livesey, and P. F.
541 Levelt (2009), Accurate satellite-derived estimates of the tropospheric ozone impact on the
542 global radiation budget, *Atmos. Chem. Phys.*, 9, 4447-4465, doi:10.5194/acp-9-4447-2009.

543

544 Joiner, J., A. P. Vasilkov, P. Gupta, P. K. Bhartia, P. Veefkind, M. Sneep, J. de Haan, I.
545 Polonsky, and R. Spurr, Fast simulators for satellite cloud optical centroid pressure retrievals;
546 evaluation of OMI cloud retrievals, *Atmos. Meas. Tech.*, 5, 529-545, doi:10.5194/amt-5-529-
547 2012, 2012.

548

549 Kley, D., P. J. Crutzen, H. G. J. Smit, et. al. (1996), Observations of near-zero ozone
550 concentrations over the convective Pacific: Effects on air chemistry, *Science*, 274, 230-233.

551

552 Levelt, P. F., et al., The Ozone Monitoring Instrument, *IEEE Trans. Geophys. Remote Sens.*,
553 44(5), 1093-1101, 2006.

554

555 Liu, H. Y., J. H. Crawford, R. B. Pierce, et al., Radiative effect of clouds on tropospheric
556 chemistry in a global three-dimensional chemical transport model, *J. Geophys. Res.*, 111 (D20),
557 D20303, 2006.

558

559 Liu, J. J. M. Rodriguez, S. D. Steenrod, A. R. Douglass, J. A. Logan, M. A. Olsen, K. Wargan,
560 and J. R. Ziemke, Causes of interannual variability over the southern hemispheric tropospheric
561 ozone maximum, *Atmos. Chem. Phys.*, 17, 3279-3299, doi:10.5194/acp-17-3279-2017, 2017.

562

563 Logan, J. A., I. Megretskaya, R. Nassar, et al., Effects of the 2006 El Nino on tropospheric
564 composition as revealed by data from the Tropospheric Emission Spectrometer (TES), *Geophys.*
565 *Res. Lett.*, 35, L03816, 2008.

566

567 Maloney, E. D., and D. L. Hartmann, Modulation of hurricane activity in the Gulf of Mexico by
568 the Madden-Julian Oscillation, *Science*, 287, 2002 – 2004, 2000.

569

570 Mo, K. C., The association between intra-seasonal oscillations and tropical storms in the Atlantic
571 Basin, *Mon. Weather Rev.*, 128, 4097–4107, 2000.

572

573 Park, C.-K., and S. D. Schubert, Remotely forced intra-seasonal oscillations over the tropical
574 Atlantic, *J. Atmos. Sci.*, 50, 89 – 103, 1993.

575

576 Sauvage, B., R. V. Martin, A. van Donkelaar, and J. R. Ziemke, Quantification of the factors
577 controlling tropical tropospheric ozone and the South Atlantic maximum, *J. Geophys. Res.*, 112
578 (D11) D11309, doi:10.1029/2006JD008008, 2007.

579

580 Solomon, S., D. W. J. Thompson, R. W. Portmann, et al., On the distribution of and variability of
581 ozone in the tropical upper troposphere: Implications for tropical deep convection and chemical-
582 dynamical coupling, *Geophys. Res., Lett.*, 32, L23813, doi:10.1029/2005GL024323, 2005.

583

584 Sneep, M., J. De Haan, P. Stammes, P. Wang, C. Vanbause, J. Joiner, A. Vasilkov, and P.
585 Levelt, Three way comparison between OMI/Aura and POLDER/PARASOL cloud pressure
586 products, *J. Geophys. Res.*, doi:10.1029/2007JD008694, 2008.

587

588 Strode, S. A., A. R. Douglass, J. R. Ziemke, M. Manyin, J. E. Nielsen, and L. D. Oman, Analysis
589 of ozone in clear versus cloudy conditions, *J. Geophys. Res.*, in review, 2017.

590

591 Vasilkov, A., J. Joiner, R. Spurr, et al., Evaluation of the OMI cloud pressures derived from
592 rotational Raman scattering by comparisons with other satellite data and radiative transfer
593 simulations, *J. Geophys. Res.*, 113, D15S19, doi:10.1029/2007JD008689, 2008.

594

595 Vömel, H., and K. Diaz, Ozone sonde cell current measurements and implications for
596 observations of near-zero ozone concentrations in the tropical upper troposphere, *Atmos. Meas.
597 Tech.*, 3, 495505, doi:10.5194/amt-3-495-2010, 2010.

598

599 Zhu, B., H. Xiao, M. Huang, and Z. Li, Numerical study of cloud effects on tropospheric ozone,
600 *Water, Air, and Soil Pollution*, 129, 199-216, 2001.

601

602 Ziemke, J. R., S. Chandra, and P. K. Bhartia, "Cloud slicing": A new technique to derive upper
603 tropospheric ozone from satellite measurements, *J. Geophys. Res.*, 106, 9853-9867, 2001.

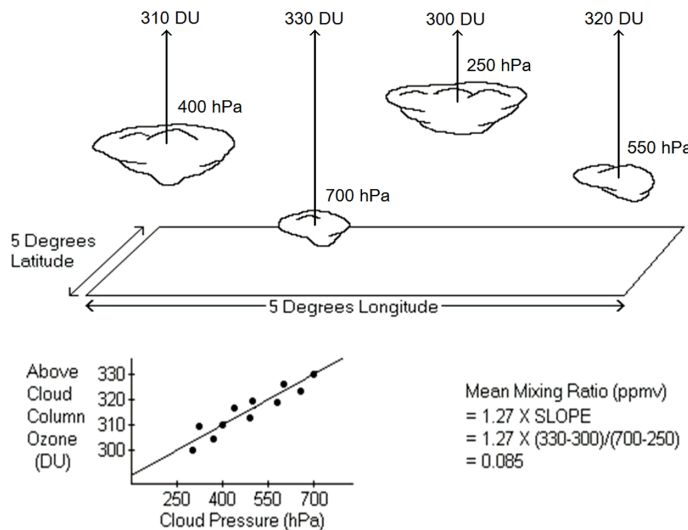
604

605 Ziemke, J. R., S. Chandra, B. N. Duncan, et al., Tropospheric ozone determined from Aura OMI
606 and MLS: Evaluation of measurements and comparison with the Global Modeling Initiative's
607 Chemical Transport Model, *J. Geophys. Res.*, 111, D19303, doi:10.1029/2006JD007089, 2006.

608

609 Ziemke, J. R., J. Joiner, S. Chandra, P. K. Bhartia, A. Vasilkov, D. P. Haffner, K. Yang, M. R.
610 Schoeberl, L. Froidevaux, and P. F. Levelt, Ozone mixing ratios inside tropical deep convective
611 clouds from OMI satellite measurements, *Atmos. Chem. Phys.*, 9, 573-583, 2009.
612
613 Ziemke, J. R., A. R. Douglass, L. D. Oman, S. E. Strahan, and B. N. Duncan, Tropospheric
614 ozone variability in the tropical Pacific from ENSO to MJO and shorter timescales, *Atmos.*
615 *Chem. Phys.*, 15, 8037-8049, doi:10.5194/acp-15-8037-2015, 2015.
616
617
618
619
620
621
622
623
624
625
626
627

"Ensemble" Cloud Slicing



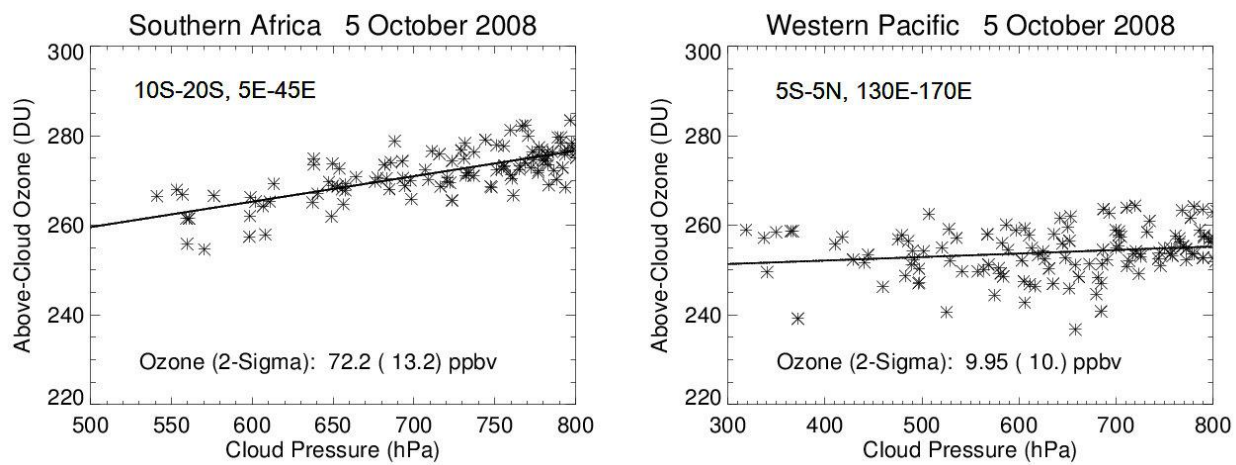
628

629 **Figure 1.** A schematic diagram illustrating the ensemble cloud slicing method involving
 630 coincident measurements of above-cloud column ozone (i.e., column ozone measured from the
 631 top of the atmosphere down to cloud pressure) and cloud pressure to measure mean volume
 632 mixing ratio (see text). For deep convective cumulonimbus clouds the cloud tops are near the
 633 tropopause and so the mean volume mixing ratio is primarily a measurement of average “in-
 634 cloud” ozone concentration. This figure was adapted from Ziemke et al. (2001). For our study
 635 all measurements are from OMI (i.e., OMI above cloud ozone versus OMI OCP).

636

637

638

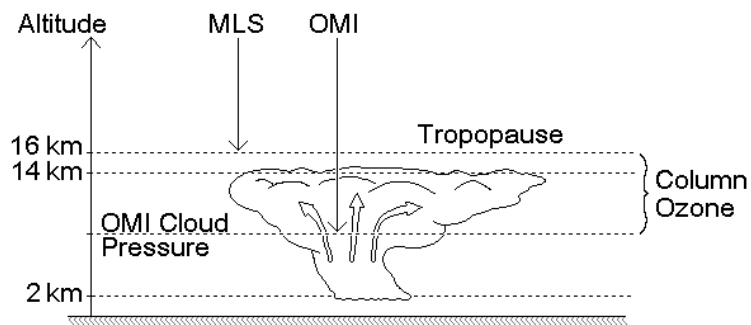


639

640 **Figure 2.** Examples of the ensemble cloud slicing technique using OMI measurements of
641 above-cloud column ozone and cloud pressure (see text).

642
643
644
645
646
647
648
649
650

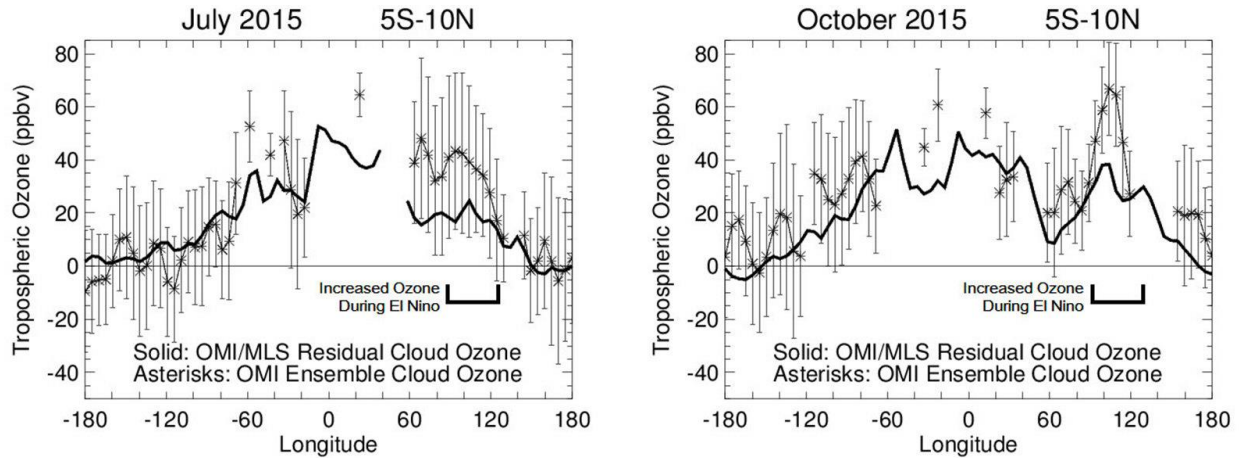
Tropospheric Column Ozone Measured Over Deep Convective Clouds



651
652 **Figure 3.** Schematic diagram of the OMI/MLS residual cloud slicing method. This depiction
653 shows that deep convective clouds have OMI cloud optical centroid pressures (OCPs) lying deep
654 inside the clouds with cloud tops often at tropopause level or very close to the tropopause. This
655 figure was adapted from Ziemke et al. (2009).

656
657
658
659

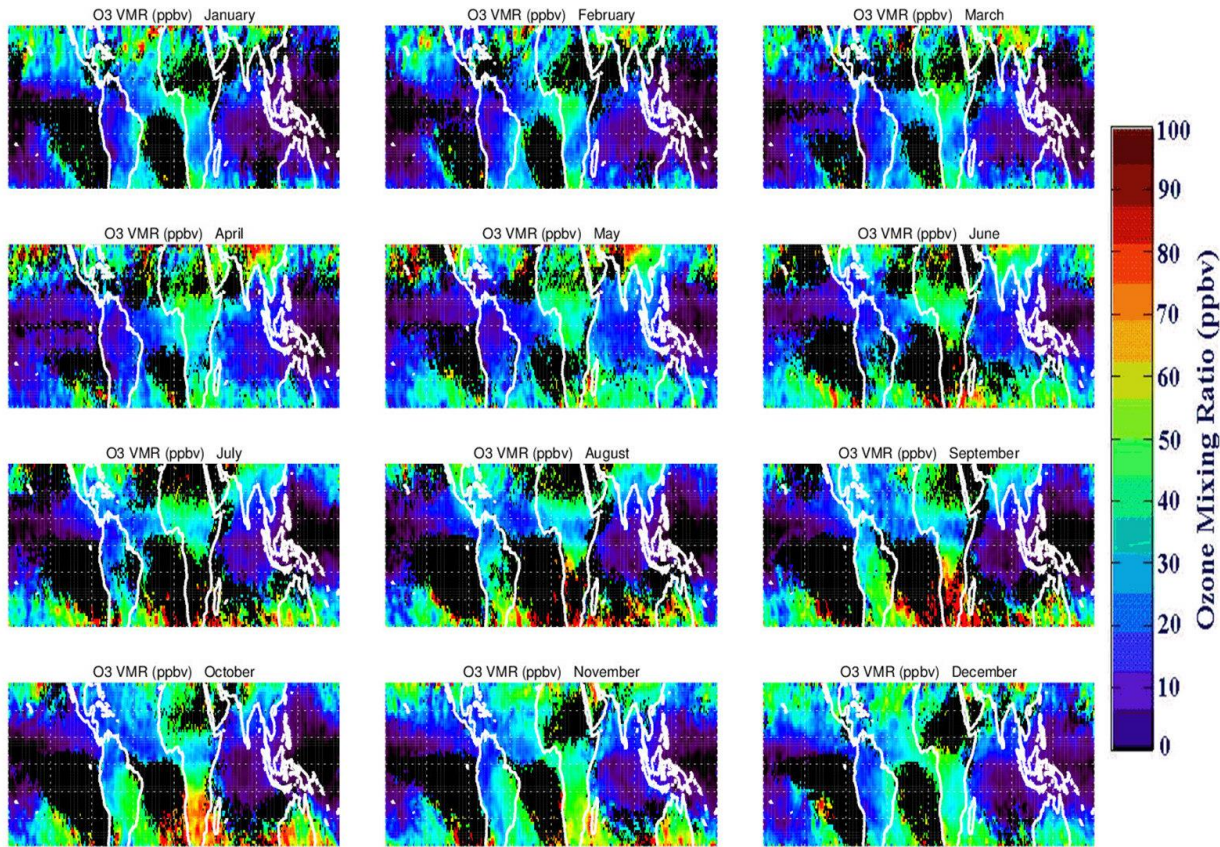
660
661
662
663



664
665 **Figure 4.** Comparisons of OMI/MLS (solid) and OMI ensemble (asterisks) cloud ozone VMR
666 for July and October 2015 with both months coinciding with the intense 2014-2016 El Nino
667 event. Measurements are averaged over the 5°S-10°N latitude band as a function of longitude (at
668 5° increments). The ensemble measurements include calculated $\pm 2\sigma$ uncertainties. Mean VMR
669 for the ensemble measurements are calculated for all OCPs lying between 250hPa and 550 hPa
670 and radiative cloud fractions $> 80\%$.

671
672
673
674
675
676
677

Cloud-Ozone Climatology

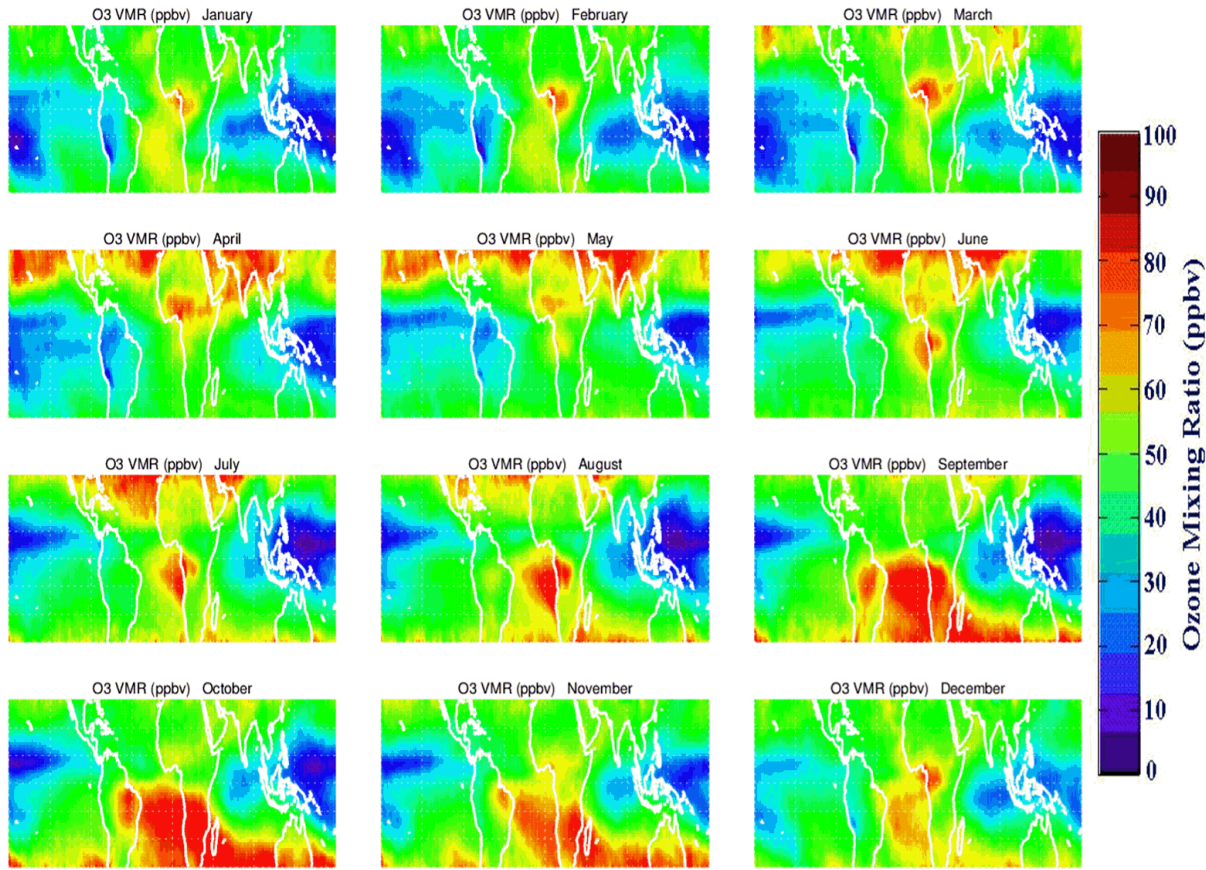


678

679 **Figure 5.** Monthly-mean climatology maps of OMI/MLS residual cloud ozone (units ppbv).
 680 Plotted is mean VMR representing average ozone concentration lying between the tropopause
 681 and OMI UV cloud pressure (OCP) as described in Section 3. The mean mixing ratio is
 682 calculated for OCPs varying between 250 hPa and 550 hPa. Black regions indicate not enough
 683 deep convective clouds present or mostly low clouds such as marine stratus clouds with OCP
 684 lying below the 550 hPa threshold.

685

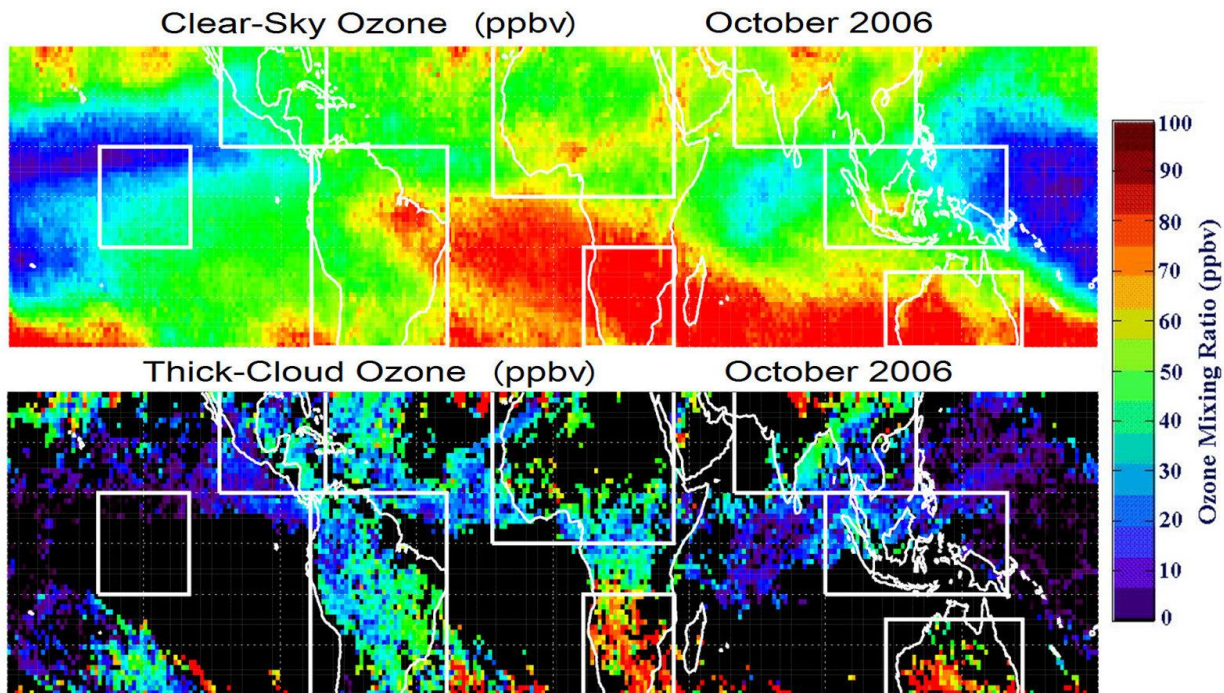
Tropospheric Ozone Climatology



686

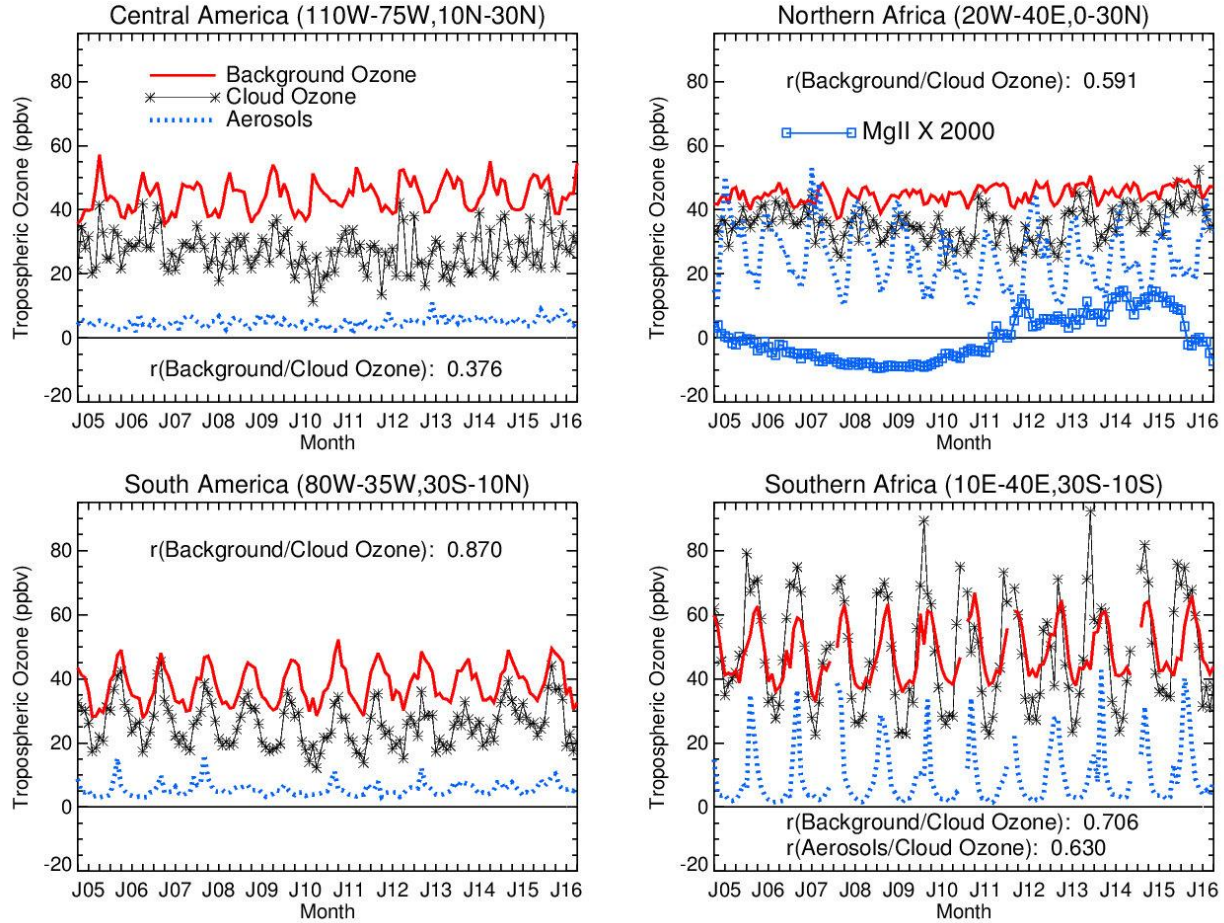
687 **Figure 6.** Similar to Figure 5, but instead plotting monthly-mean climatology maps of
688 OMI/MLS VMR (units ppbv) for OMI near clear-sky scenes (i.e., radiative cloud fractions less
689 than 30%).

690



691
692 **Figure 7.** (Top) Background (near clear-sky) tropospheric ozone in units ppbv for October
693 2006. Shown as white rectangles are eight selected regions of interest where measurements are
694 averaged each month to generate long record time series for October 2004 – April 2016.
695 (Bottom) Same as top but instead for cloud ozone.

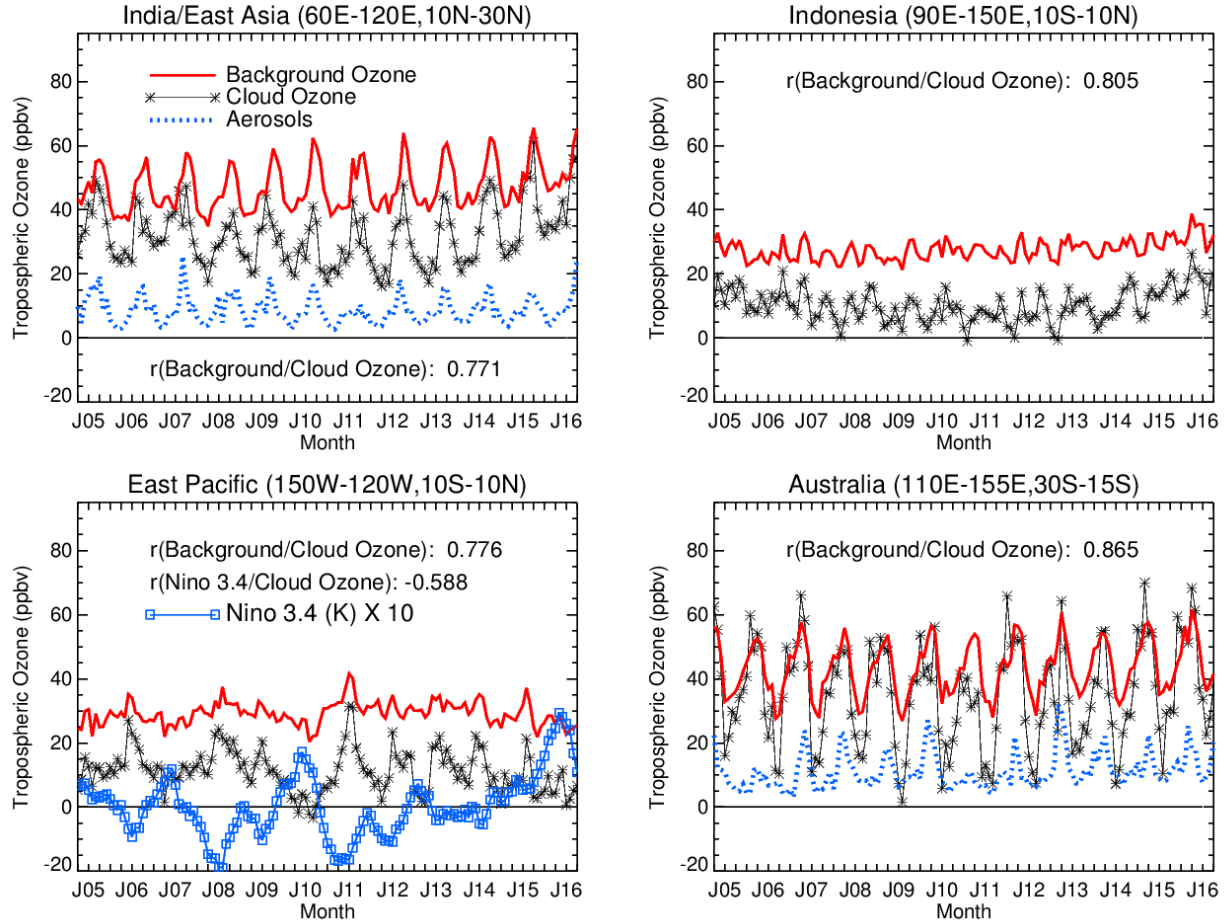
696
697



698

699 **Figure 8.** Monthly time series of background ozone (thick solid red curves) and cloud ozone
700 (thin black curves with asterisks) for the regions of Central America, South America, northern
701 Africa, and southern Africa in Figure 7. All ozone units are ppbv. Also shown for each of these
702 landmass regions is the OMI monthly aerosol index time series (dotted blue curves, no units)
703 which was re-scaled (i.e., multiplied by 60) for plotting. Included for the northern Africa region
704 is the solar MgII index (SI units) that has been re-scaled for plotting (i.e., time average removed
705 and then multiplied by 2000). The correlation between background ozone and cloud ozone is
706 indicated in each panel. Also included for southern Africa is correlation between aerosol index
707 and cloud ozone.

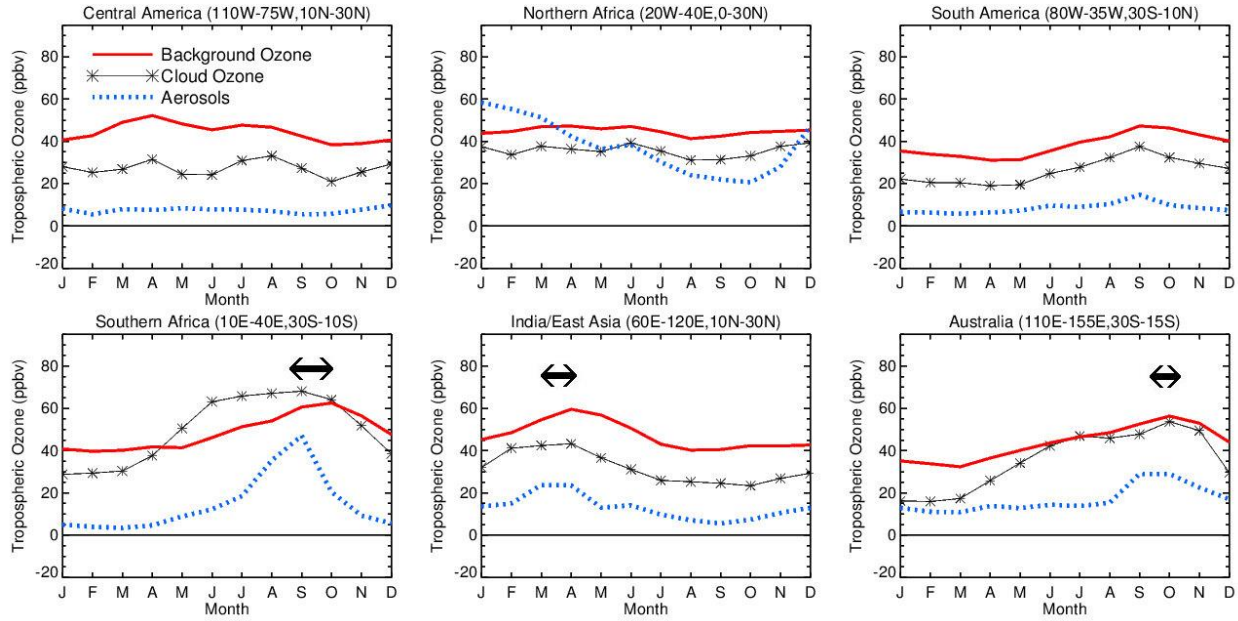
708



709

710 **Figure 9.** Similar to Figure 8, but instead for the regions of India/east Asia, Indonesia, eastern
 711 Pacific, and Australia. Aerosol index time series (dotted) for the landmass regions is again
 712 shown. Also included for the eastern Pacific (lower left panel) is the Nino 3.4 index (blue
 713 squares, units K) and its correlation with cloud ozone. The Nino 3.4 index was re-scaled
 714 (multiplied by 10) for plotting with ozone time series.

715



716
717
718
719
720
721
722

Figure 10. Twelve-month climatology time series for the six continental land-mass regions plotted in Figures 8 and 9 using the same color scheme. Shown here are background ozone (solid red curves), cloud ozone (asterisks), and aerosol index (dotted blue curves). The OMI aerosol index has been re-scaled (i.e., multiplied by 60) for plotting. Approximate phase shifts between background ozone and aerosol index time series are shown with dark arrows.